

Two-Dimensional Intravascular Near-Infrared Fluorescence Molecular Imaging of Inflammation in Atherosclerosis and Stent-Induced Vascular Injury

Farouc A. Jaffer, MD, PhD,*† Marcella A. Calfon, MD, PhD,* Amir Rosenthal, PhD,*||
Georgios Mallas, MSc,*¶ R. Nika Razansky, PhD,|| Adam Mauskapf, BS,*
Ralph Weissleder, MD, PhD,†‡ Peter Libby, MD,§ Vasilis Ntziachristos, PhD||

Boston, Massachusetts; and Munich, Germany

Objectives This study sought to develop a 2-dimensional (2D) intravascular near-infrared fluorescence (NIRF) imaging strategy for investigation of arterial inflammation in coronary-sized vessels.

Background Molecular imaging of arterial inflammation could provide new insights into the pathogenesis of acute myocardial infarction stemming from coronary atheromata and implanted stents. Presently, few high-resolution approaches can image inflammation in coronary-sized arteries *in vivo*.

Methods A new 2.9-F rotational, automated pullback 2D imaging catheter was engineered and optimized for 360° viewing intravascular NIRF imaging. In conjunction with the cysteine protease-activatable imaging reporter Prosense VM110 (VisEn Medical, Woburn, Massachusetts), intra-arterial 2D NIRF imaging was performed in rabbit aortas with atherosclerosis ($n = 10$) or implanted coronary bare-metal stents ($n = 10$, 3.5-mm diameter, day 7 post-implantation). Intravascular ultrasound provided coregistered anatomical images of arteries. After sacrifice, specimens underwent *ex vivo* NIRF imaging, fluorescence microscopy, and histological and immunohistochemical analyses.

Results Imaging of coronary artery-scaled phantoms demonstrated 8-sector angular resolution and submillimeter axial resolution, nanomolar sensitivity to NIR fluorochromes, and modest NIRF light attenuation through blood. High-resolution NIRF images of vessel wall inflammation with signal-to-noise ratios >10 were obtained in real-time through blood, without flushing or occlusion. In atherosclerosis, 2D NIRF, intravascular ultrasound–NIRF fusion, microscopy, and immunoblotting studies provided insight into the spatial distribution of plaque protease activity. In stent-implanted vessels, real-time imaging illuminated an edge-based pattern of stent-induced arterial inflammation.

Conclusions A new 2D intravascular NIRF imaging strategy provides high-resolution *in vivo* spatial mapping of arterial inflammation in coronary-sized arteries and reveals increased inflammation-regulated cysteine protease activity in atheromata and stent-induced arterial injury. (J Am Coll Cardiol 2011;57:2516–26) © 2011 by the American College of Cardiology Foundation

Thrombotic complications of atherosclerosis and implanted coronary stents include myocardial infarction and sudden cardiac death. Accordingly, there exists a compelling need

to identify patients that harbor thrombosis-prone plaques and/or implanted stents, as well as to monitor interventions aimed at their mitigation. At present, however, clinicians

From the *Cardiovascular Research Center and Cardiology Division, Massachusetts General Hospital, Harvard Medical School, Boston, Massachusetts; †Center for Molecular Imaging Research, Massachusetts General Hospital, Harvard Medical School, Boston, Massachusetts; ‡Center for Systems Biology, Massachusetts General Hospital, Boston, Massachusetts; §Cardiovascular Division, Brigham and Women's Hospital, Harvard Medical School, Boston, Massachusetts; ||Institute for Biological and Medical Imaging, Helmholtz Zentrum München und Technische Universität München, Munich, Germany; and the ¶Department of Electrical and Computer Engineering, Northeastern University, Boston, Massachusetts. This work was supported by National Institutes of Health grants #R01 HL 108229 (to Dr. Jaffer) and #R01 HL 80472 (to Dr. Libby), American Heart Association Scientist Development

Grant #0830352N (to Dr. Jaffer), Howard Hughes Medical Institute Career Development Award (to Dr. Jaffer), Broadview Ventures (to Drs. Jaffer and Ntziachristos), Donald W. Reynolds Foundation (to Drs. Jaffer, Weissleder, and Libby), European Community's Seventh Framework Programme (FP7/2007–2013 under grant agreement #235689 [to Dr. Rosenthal]), and MGH William Schreyer Fellowship (to Dr. Calfon). Dr. Jaffer has been a consultant to VisEn Medical; and received a research grant from Abbott Vascular. Dr. Weissleder has been a consultant to and has an equity interest in VisEn Medical. All other authors have reported that they have no relationships to disclose. Drs. Jaffer and Calfon contributed equally to this work.

Manuscript received November 11, 2010; revised manuscript received January 25, 2011, accepted February 15, 2011.

lack the tools to gauge biological aspects of atheromata and stented arteries.

The biological characteristics of the arterial wall critically influence atherogenesis and plaque thrombosis (1,2), as well as the hyperplastic and thrombotic complications of arterial stenting (3,4). Molecular imaging strategies now afford an approach to reach beyond anatomy and visualize *in vivo* atheroma inflammation, angiogenesis, apoptosis, oxidative stress, and calcification (5,6). Yet, although, clinically feasible for larger vessels such as the carotid and the aorta, high-resolution clinical molecular imaging strategies for the coronary arteries remain scarce, primarily due to the small imaging target volume, and multiple sources of image degradation, including cardiac and respiratory motion, and blood flow.

In vivo near-infrared fluorescence (NIRF) visualization approaches appear attractive for human coronary arterial molecular imaging (7). A recent preliminary study demonstrated 1-dimensional (1D) NIRF sensing (nonimaging) of atheroma inflammation in small diameter (1.5 to 2.0 mm) vessels (8). This approach, however, did not enable 2-dimensional (2D) imaging, nor sense NIRF signals in vessels of diameters more typical of human coronary arteries (2.5 to 3.5 mm), nor evaluate inflammation due to coronary stent-induced injury. Additional limitations of the nonrotational 1D spectroscopic instrument included NIRF signal detection from only a small sector of the entire 360° arterial wall, limiting its sensitivity. In addition, the 1D system

lacked longitudinal (axial) anatomical accuracy due to manual pullback and was subject to loss of distal vessel access due to required pullback of the sensing guidewire (as opposed to standard catheter-based imaging approaches).

To address these limitations and to advance the clinical potential of intracoronary NIRF molecular imaging, we present a new 2D rotational and automated pullback NIRF intravascular catheter apparatus, capable of nanomolar-sensitive, intra-arterial molecular imaging in larger diameter coronary arteries. We use the 2D NIRF catheter to provide new biological insights into arterial inflammation in atheroma and coronary stent-induced vascular injury *in vivo*.

Abbreviations and Acronyms

1D = 1-dimensional

2D = 2-dimensional

FRI = fluorescence reflectance imaging

IVUS = intravascular ultrasound

NIRF = near-infrared fluorescence

ROI = region of interest

SNR = signal-to-noise ratio

TBR = target-to-background ratio

VM110 = ProSense VM110 imaging agent

Methods

Two-dimensional NIRF imaging device and catheter. The apparatus (Fig. 1, Online Fig. 1) houses a continuous-wave laser source operating at 750 nm (B&W Tek Inc., Newark, Delaware) with electronically adjustable output

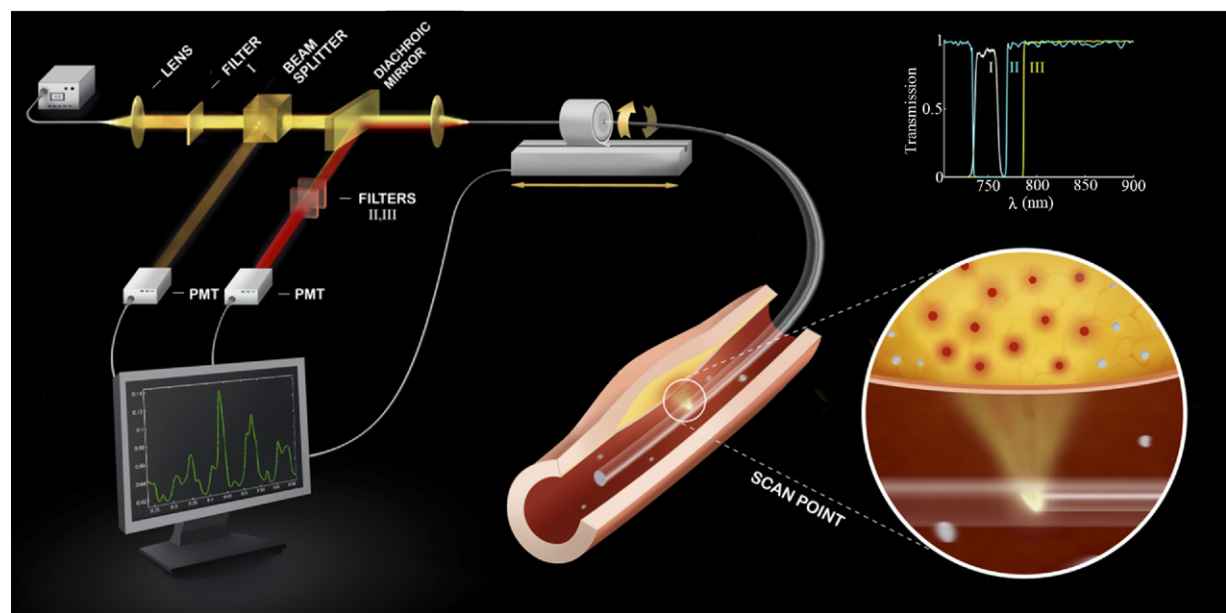


Figure 1 Schematic of the Constructed 2D NIRF Imaging System

The tip of the fiber contains a right angle coated prism that reflects the guide's laser light into the artery wall and couples the subsequent fluorescent light back into the fiber. The fluorescent light is then directed to a dichroic beam splitter that selectively reflects it into a photomultiplier tube. The beam passes additional filters to minimize the parasitic signals of laser photons and autofluorescence. The inset shows the spectra of the 3 filters (I, II, III) used in the system. 2D = 2-dimensional; NIRF =

power. The catheter consists of an optical fiber (numerical aperture 0.37) within a polyethylene sheath (outer diameter 2.9-F) that guides the 750 nm laser light and collects the subsequent NIRF emission. The fiber is rotated and translated using mechanical stages to collect fluorescence and generate a 2D NIRF image. See Online Appendix for supplemental methods, including phantom experiments.

Cysteine protease activity NIRF molecular imaging agent. To image cysteine protease activity, an activatable NIRF imaging agent (Prosense VM110 [VM110], 0.5 mg/kg, excitation/emission, 750 nm/780 nm, VisEn Medical, Woburn, Massachusetts) was scaled up for use in atherosclerosis and arterial stent injury in rabbits. This class of protease-activatable agents has been extensively validated, and cysteine protease activity, in particular cathepsin B, has been reported on (8–10).

Rabbit atherosclerosis. Atherosclerotic lesions rich in inflammatory cells in New Zealand white rabbits were induced by balloon injury and hypercholesterolemic diet as performed previously (8). Intravascular 2D NIRF imaging of atheroma inflammation ($n = 10$; $n = 7$ VM110, $n = 3$ saline) was performed at 8 weeks after injury. An additional control group consisted of normal rabbits ($n = 2$) injected with VM110 (0.5 mg/kg) 24 h before imaging.

Stent-induced arterial injury. Bare-metal coronary stents (3.5-mm diameter \times 12-mm length) were implanted into the aorta of rabbits ($n = 10$). Intravascular 2D NIRF imaging of stent-induced inflammation was performed at 7 days after injury, 24 h after receiving Prosense VM110 ($n = 8$, 0.5 mg/kg) or saline ($n = 2$). See the supplemental methods in the Online Appendix.

Intravascular NIRF and IVUS imaging. On the day of imaging, animals were anesthetized as described in the supplemental methods (Online Appendix). A 5-F introducer was inserted into the right carotid artery using fluoroscopic and angiographic guidance. Iodinated contrast was injected and baseline x-ray angiography was recorded using standard cineangiography. An intravascular ultrasound (IVUS) catheter was inserted over a 0.014-inch guidewire and serial pullbacks were performed (Galaxy IVUS System, Boston Scientific/Scimed, Inc., Natick, Massachusetts) from the iliac bifurcation to the renal arteries, with a pullback length of 100 mm. Next, the monorail NIRF catheter was advanced over the guidewire. To cover the entire IVUS-imaged vessel and understand reproducibility of the NIRF signal profiles, the NIRF catheter was advanced into the iliac artery and 3 to 4 contiguous, 110-mm length pullbacks were performed (rotational speed 30 to 100 rev/min). Animals were then euthanized and the iliac and aorta were resected. The NIRF catheter was gently reintroduced into lumen of the aorta and ex vivo NIRF pullbacks were repeated up to 3 times. Corresponding images were aligned using iliac bifurcation and renal arteries as landmarks, and radiopaque catheter markers as fiducials. Areas of plaque and normal vessel were confirmed by IVUS images.

Fluorescence reflectance imaging. Resected vessels underwent multiple wavelength fluorescence reflectance imag-

ing (FRI) (OV110, Olympus, Tokyo, Japan), equipped with an NIR filter set (Omega Optical, Brattleboro, Vermont): bandpass excitation: 716 to 756 nm, bandpass emission: 780 to 820 nm. Multiple exposure times (0.1 to 60 s) for each wavelength and acquired images were exported as DICOM (Digital Imaging and Communications in Medicine) files for further analysis. Due to vessel shrinkage after resection, the aorta and the iliac vessels were manually elongated to in vivo measured lengths. Regions of interest (ROIs) were traced manually after visual identification of normal vessel, background, plaque, and stented zones (Osirix version 2.7.5, Pixmeo, Switzerland). Stent ROIs included 3 mm of tissue at the proximal and distal edge, respectively (total length of ROI drawn was 18 mm for 12-mm stent). Target-to-background ratios (TBRs) were calculated for each ROI by dividing the mean ROI signal of target by adjacent vessel background (normal vessel). For SNR calculations, the mean ROI signal of target was divided by the standard deviation of background signal for each image.

Fluorescence microscopy. Fluorescence microscopy of plaque and normal vessel sections was performed on adjacent sections from fresh-frozen rabbit arteries, and the images were captured and processed using an epifluorescence microscope (Eclipse 80i, Nikon Instruments, Melville, New York) with filter sets for NIRF (excitation: 673 to 684 nm; dichroic mirror: DM750; emission: 765 to 835 nm; exposure time: 30 s) and autofluorescence (excitation: 460 to 500 nm; dichroic mirror: DM505; emission: 510 to 560 nm; exposure time: 1 s).

Statistical analyses. In vivo signal-to-noise ratio (SNR) and TBR values were reported as median and quartiles (25th percentile, 75th percentile) (Prism 5.0c, GraphPad, La Jolla, California). Statistically significant differences between 2 groups were determined using the Mann-Whitney *U* test for unpaired observations, and the Wilcoxon matched-pairs signed-ranks test for paired observations. Among multiple groups, significance was assessed via the Kruskal-Wallis test. A *p* value of <0.05 was considered statistically significant.

See the Online Appendix for supplemental methods for in vivo atherosclerosis and stent NIRF SNR and TBR measurements, NIRF-IVUS image fusion, histopathology, and immunoblotting.

Results

In vitro evaluation of a nanomole-sensitive rotational, automated pullback catheter platform for intravascular NIRF molecular imaging. In vitro performance (image generation, sensitivity, axial resolution, angular resolution) of the 2D NIRF system was tested in custom-built coronary-scale phantoms (Online Fig. 2). We first obtained SNR measurements for various fluorochrome concentrations immersed in saline and bloodlike solution, respectively (Figs. 2A and 2B). In saline, a 100-nmol/l fluorochrome concentration was detected at fiber-to-target distances of up to 4.5 mm. In the bloodlike solution, the detected NIRF signal decayed exponentially with

distance ($d_{1/2} = 0.33$ mm). The 50 $\mu\text{mol/l}$ and 100 nmol/l NIRF phantoms were detected at fiber-to-target distances of up to 2.5 and 1.2 mm, respectively. The overall system sensitivity improved by an order of magnitude compared with an earlier 2D prototype (11).

In saline, the angular resolution, or the ability to discern discrete sectors along the circumference of the vessel, ranged from 24° to 29° and was relatively unaffected by distance (Fig. 2C). The angular resolution was lower in the bloodlike solution (35° to 42°) due to light scattering, but still demonstrated the ability to resolve >8 sectors at a fiber-to-target distance of 3.0 mm. The axial resolution, or ability to resolve fluorescence signals along the long axis of the vessel, varied as a function of the fiber-to-target distance (Fig. 2D). In blood, the resolution depended nonlinearly on the fiber-to-target distance, reaching 1.0-mm resolution at a 2.0-mm fiber-to-target distance.

Intravascular NIRF high-resolution imaging of protease activity in rabbit atheromata in blood-filled arteries. The validated 2D NIRF catheter was then used to generate 2D geometrically accurate maps of inflammation in atheroscle-

rosis. Twenty-four hours after injection of Prosense VM110 ($n = 7$) or saline ($n = 3$), atherosoma-bearing rabbits ($n = 10$) underwent multimodality x-ray angiography, IVUS, and in vivo NIRF imaging. In atherosclerotic animals injected with VM110, in vivo NIRF catheter imaging revealed intense focal signals along pullbacks, indicating elevated cysteine protease activity (Fig. 3A). Ex vivo FRI confirmed high NIRF signals within plaques (Figs. 3B and 3C). In contrast, both saline-injected atherosclerotic and normal, VM110-injected animals demonstrated reduced NIRF signals on in vivo and ex vivo NIRF imaging (Figs. 3D to 3I). The ex vivo vessel SNR was significantly greater in VM110-injected atherosoma-bearing rabbits than control atherosoma/saline rabbits and control normal/VM110 rabbits (median [quartiles]: 229.1 [154.3, 311.6] vs. 90.2 [76.3, 90.5] and 83.6 [70.9, 96.2], $p = 0.01$) (Fig. 4A). In the 2 atherosclerosis groups (Figs. 4B and 4C), the ex vivo plaque SNR and TBR were >140% higher in the VM110 group than in the saline group (median [quartiles]: plaque SNR: 218.5 [194.3, 348.0] vs. 90.5 [77.9, 90.9], $p = 0.01$; plaque TBR: 2.4 [2.0, 3.3] vs. 1.0 [1.0, 1.1], $p = 0.01$).

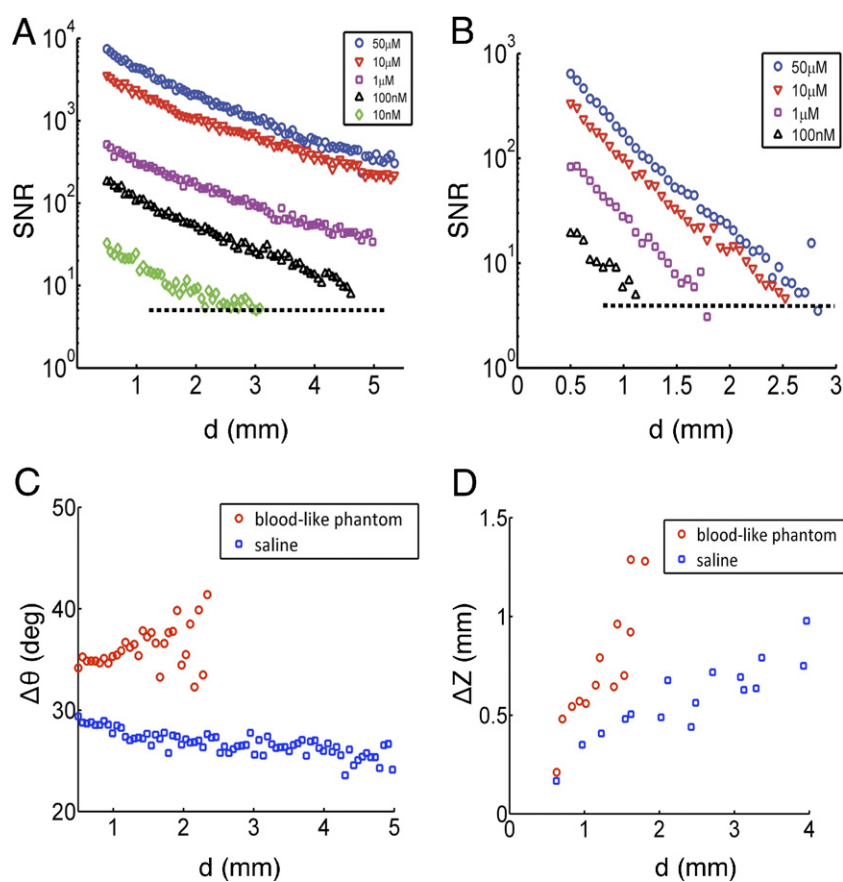
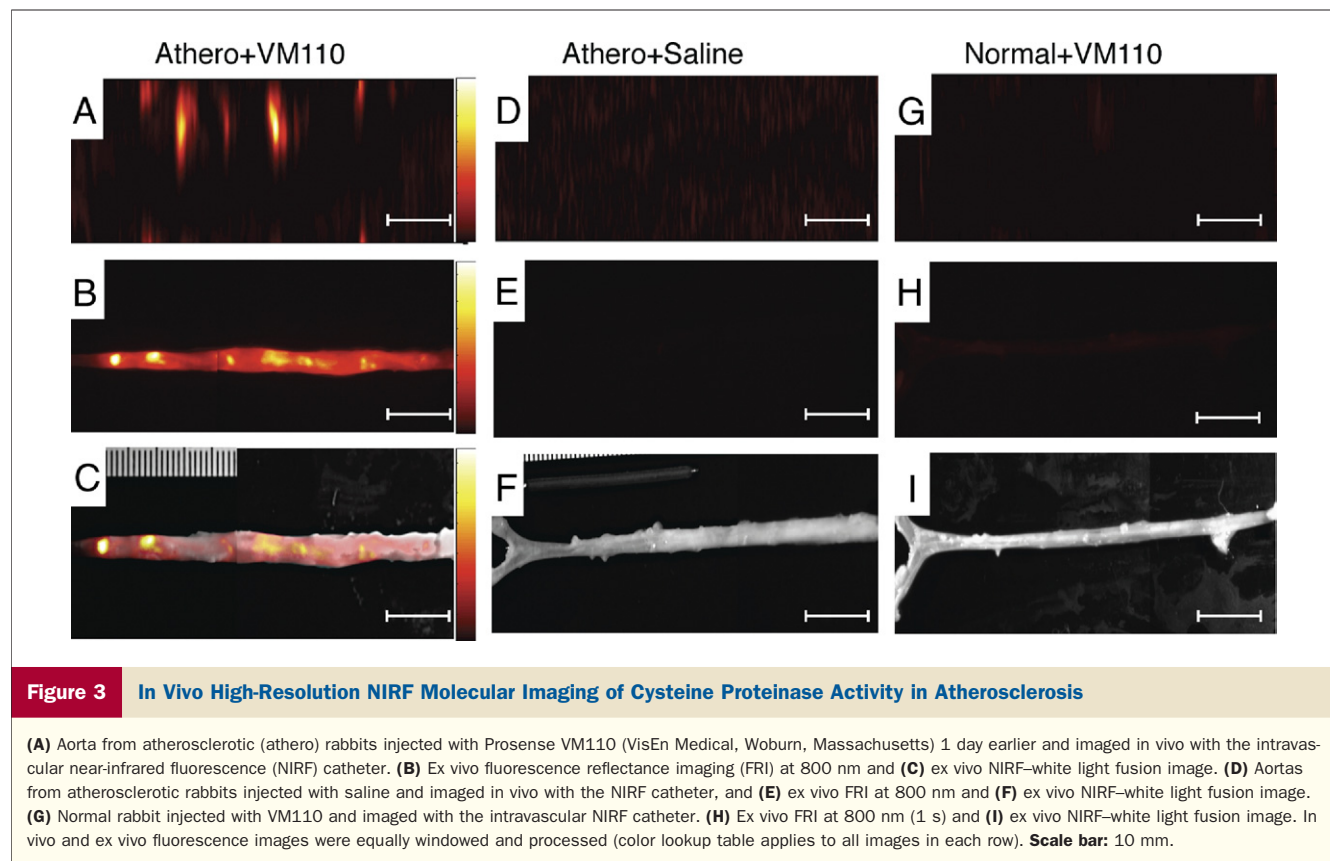


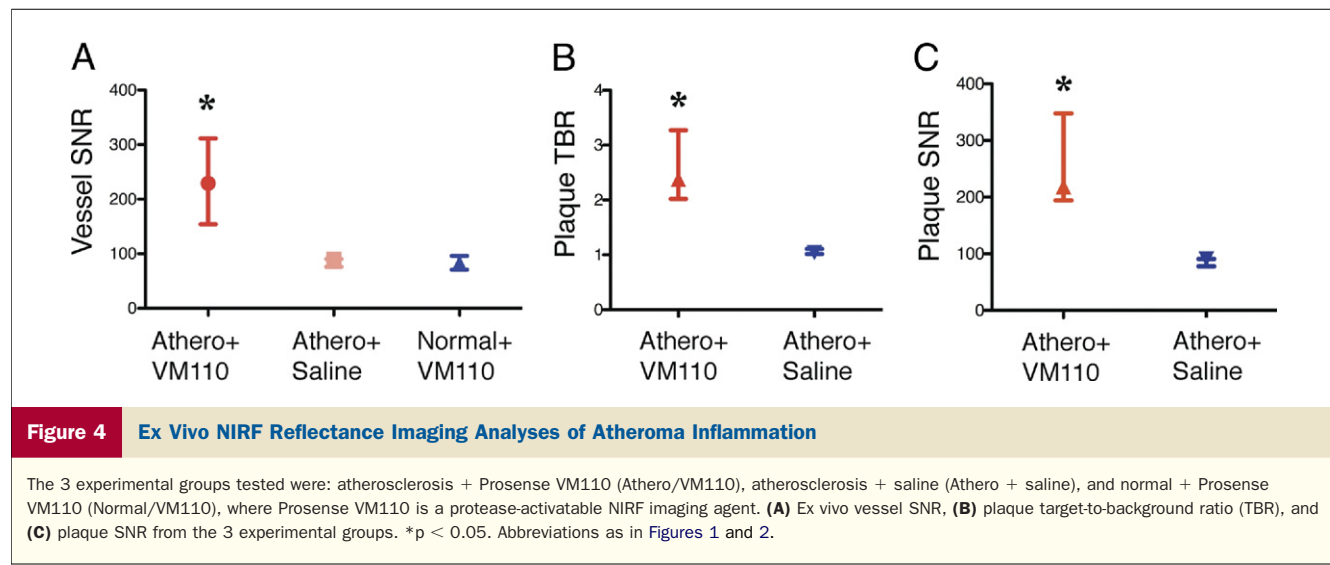
Figure 2 Evaluation of the 2D NIRF Apparatus in Coronary Artery Scale Phantoms

The signal-to-noise ratio (SNR) of the catheter for different fluorochrome concentrations measured in (A) saline and (B) bloodlike solutions. (C) Angular and (D) axial resolution of the system in saline and bloodlike solutions. The dashed line in A and B designates the sensitivity limit of the system, corresponding to SNR = 4. d is the distance from catheter-to-target; the fiber-to-target distance equals $d + 0.5$ mm. Abbreviations as in Figure 1.



Radiopaque markers and vascular fiducials allowed reliable coregistration of intravascular NIRF and IVUS images and demonstrated NIRF signal in areas of IVUS-demarcated atherosclerosis (Fig. 5). Focality of NIRF signal enhancement was appreciable in both the angular and axial dimensions (Figs. 5D and 5E), which is consistent with the eccentric, multifocal profile of IVUS-verified atherosclerosis. Areas of normal-appearing vessel (lack of plaque detected by IVUS) demonstrated little NIRF

background signal. The Prosense VM110 group showed significantly higher vessel SNR in vivo, with >170% increase over to the other 2 control groups ($p = 0.04$) (Fig. 6A). In rabbits with atheromata, the in vivo plaque SNR and TBR was >450% higher in the VM110 group than in the saline group (median [quartiles]: SNR: 12.6 [8.1, 20.6] vs. 1.3 [0.9, 2.1], $p = 0.02$; TBR: 6.3 [4.3, 9.4] vs. 1.1 [0.9, 1.4], $p = 0.02$) (Figs. 6B and 6C). In addition, augmented NIRF proteinase signal also ap-



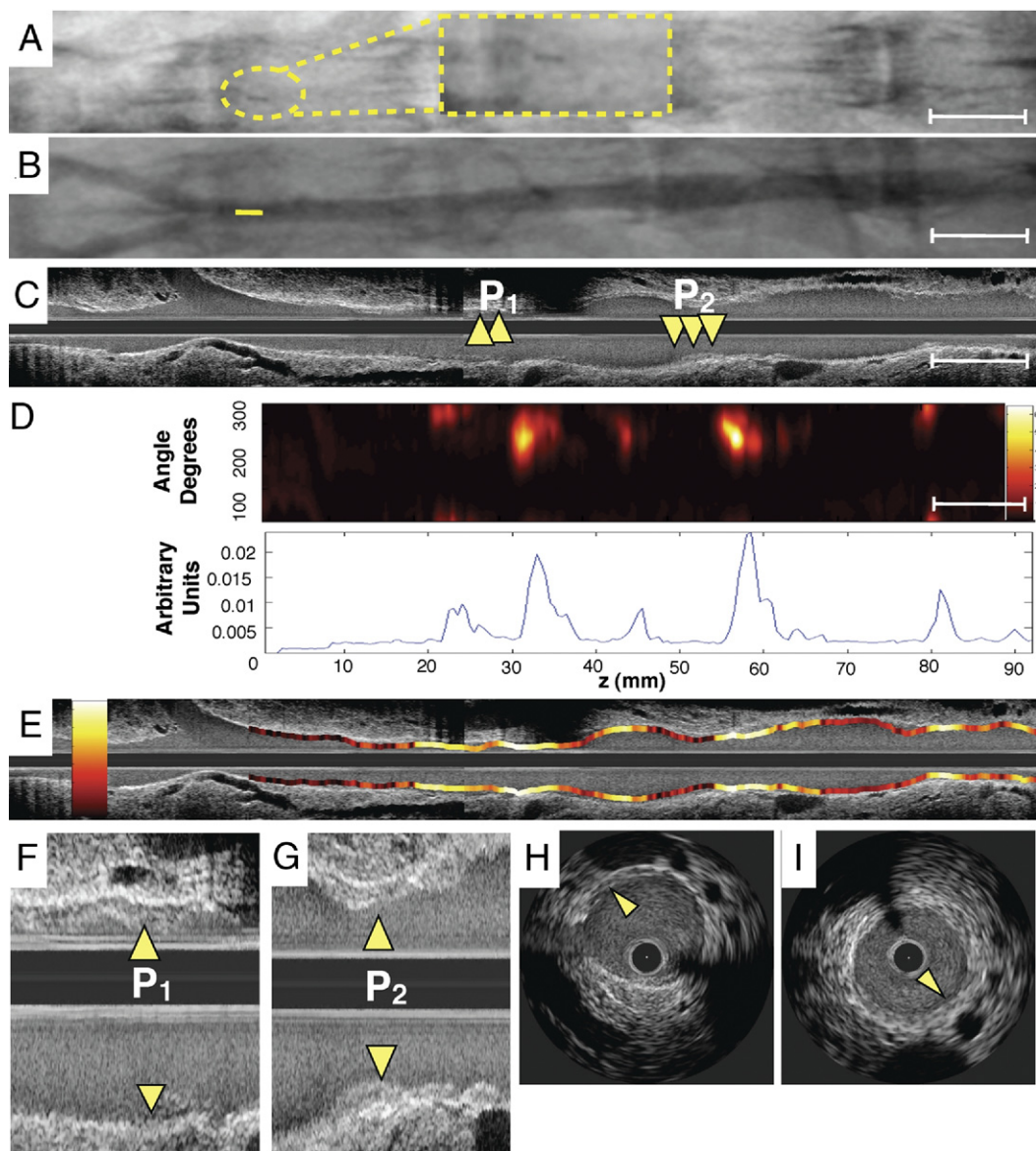


Figure 5 Representative In Vivo Molecular and Anatomical Imaging of Inflamed Atheromata

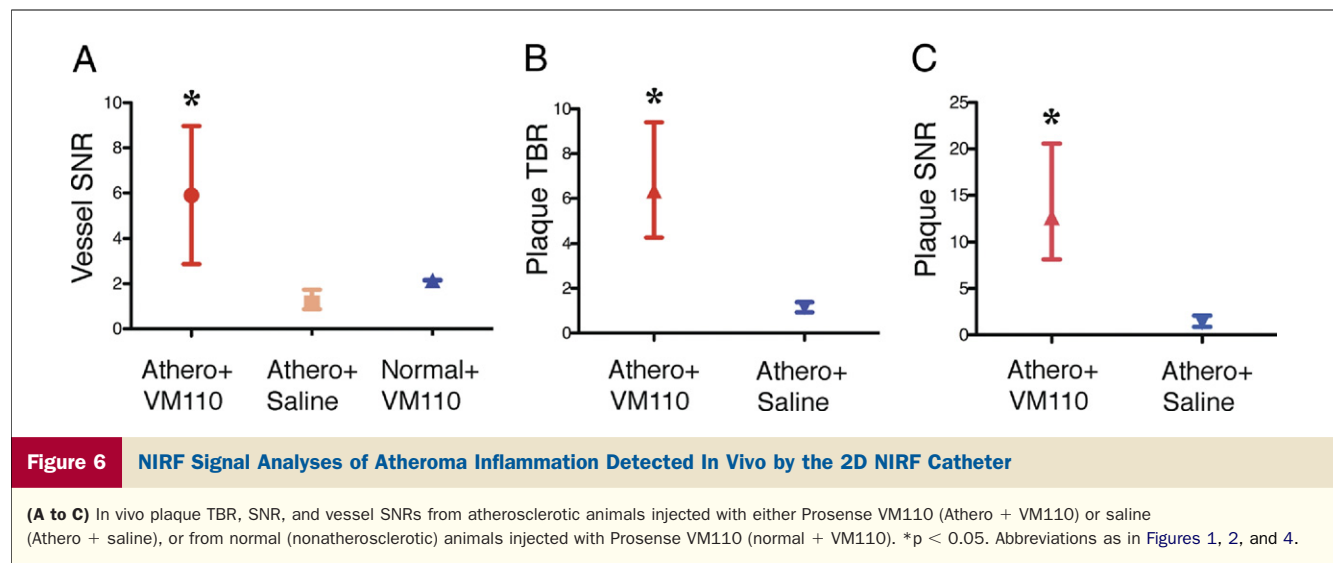
(A) Angiographic appearance (with inset high magnification image in dotted yellow lines) of radiopaque tip of NIRF catheter positioned just proximal to the iliac bifurcation, enabling coregistration with intravascular ultrasound (IVUS). (B) Angiogram of the atherosclerotic iliac and aorta. Tip of the NIRF catheter at pullback initiation confirming its intravascular position (yellow). (C) Longitudinal IVUS image of the abdominal aortoiliac arteries. Arrows demarcate IVUS-detectable mildly stenotic plaques (P_1 , P_2). (D) Image of NIRF catheter pullback aligned with the angiogram and IVUS image demonstrates NIRF signal in small volume plaques, in >3.0 -mm-diameter arteries. Corresponding 1-dimensional plot of the angle-averaged 2D NIRF intensity pullback below. (E) Longitudinal superimposed NIRF and IVUS fusion images (yellow/white = strongest NIRF signal intensity, red/black = lowest NIRF signal intensity). (F, G) High magnification image of plaque zones P_1 and P_2 . Arrows indicate minimally stenotic atherosclerotic plaques. (H, I) Axial IVUS images from zone P_1 and P_2 . Abbreviations as in Figure 1.

peared in an area of injury-induced arterial dissection adjacent to atheroma (Online Fig. 3).

Elevated in vivo and ex vivo plaque NIRF signal associates with the cysteine protease cathepsin B. Advanced plaques and early plaques (Figs. 7A and 7B) demonstrated strong cathepsin B immunoreactivity within the intima and media, consistent with augmented proteinase expression (precursor and mature form) within macrophages and

smooth muscle cells (12,13). Intimal cathepsin B staining colocalized with immunohistochemical detection of RAM-11 positive intimal macrophages. In contrast, the normal vessel wall produced minimal cathepsin B and macrophage staining (Fig. 7C).

Fluorescence microscopy revealed focal NIR fluorescence in the intima of advanced plaques (Fig. 7A). Early atherosoma with cathepsin B enzyme presence (Fig. 7B) did not



emit NIRF, which suggests lower cysteine protease activity in early stage plaques. Fluorescence microscopy further revealed that the NIRF signal was plaque-specific and VM110-specific, as autofluorescence signal (535-nm fluorescence) colocalized with elastin-rich medial fiber signals. Slight medial autofluorescence was visualized in the 800-nm channel and, as expected, was substantially lower than autofluorescence at 535 nm (14,15). Immunoblotting of

normal and plaque-rich aorta showed increased expression of both precursor and mature cathepsin B protein in plaque-rich vessels (Fig. 7D).

Intravascular NIRF molecular imaging of coronary stent-induced arterial inflammation reveals a stent edge-based injury pattern in vivo. Extended arterial inflammation characterizes unhealed coronary stents that may provoke stent thrombosis (3,4). To investigate and image

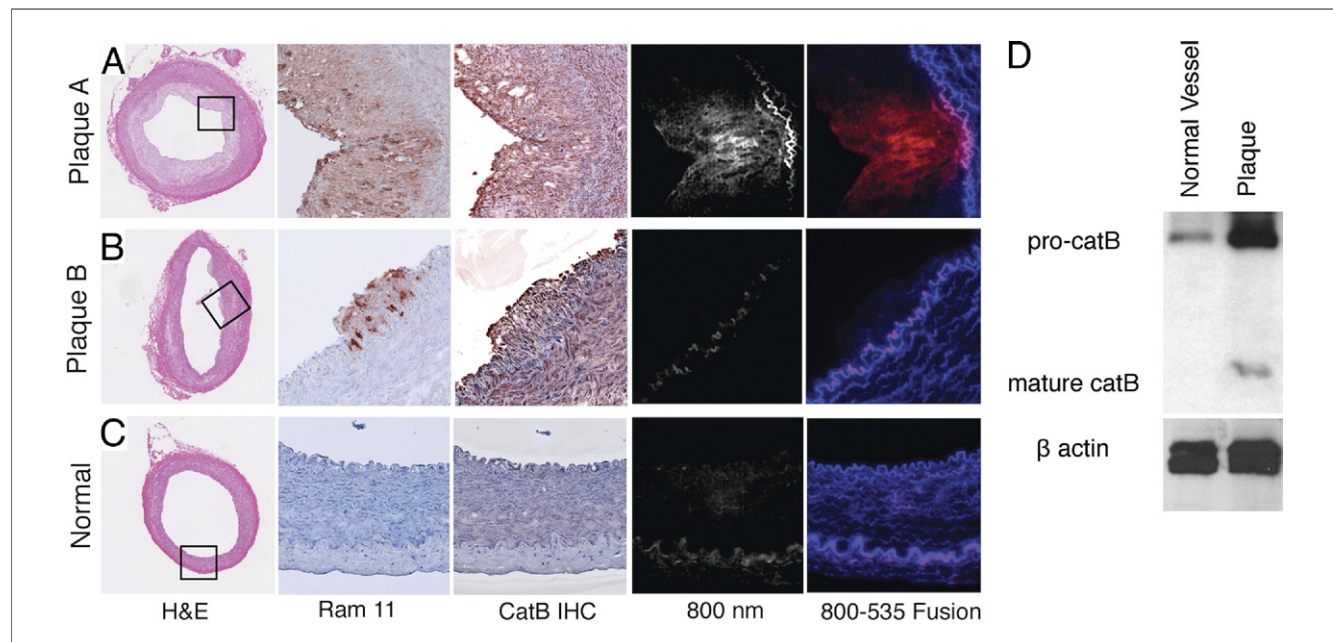


Figure 7 Histopathological and Immunoblotting Assessments of Aortic Inflammation

In each row, the 5 images depict correlative arterial sections of hematoxylin and eosin (H&E) staining (10 \times), immunoreactive macrophages (RAM-11, 20 \times), immunoreactive cathepsin B (catB, 20 \times), near-infrared fluorescence (NIRF) at 800 nm, and merged 800-nm–535-nm fluorescence, with red color denoting 800-nm signal induced by cysteine protease activation of Prosense VM110, and blue color denoting signal at 535 nm originating from autofluorescence. (A) In an advanced plaque, immunoreactive macrophages and cathepsin B, and intimal NIRF protease activity signals are evident. (B) Early stage atheroma demonstrates macrophages and cathepsin B in the intima and media but little NIRF cysteine protease activity (800-nm image). (C) Section of a normal artery. Elastin fibers provide a source of autofluorescence (blue color) on fusion fluorescence microscopy images. (D) Cathepsin B and beta-actin immunoblot of lysates from normal and plaque-containing vessel demonstrates cathepsin B in atherosclerotic aortas. Pro-catB denotes the 46 kD pre-cathepsin B band, and mature catB denotes the 25 kD and 30 kD cathepsin B bands.

arterial wall inflammation *in vivo* following stent deployment, New Zealand White rabbits underwent aortic balloon injury ($N = 10$) followed by deployment of a bare-metal coronary stent (3.5×12 mm). Six days following stent implantation, rabbits received intravenous Prosense VM110 ($n = 8$) or saline ($n = 2$). The next day (day 7) rabbits underwent *in vivo* multimodality x-ray angiography, IVUS, and intravascular NIRF imaging. In stent-injured vessels, increased *in vivo* NIRF signal localized at the edges of the implanted stents, and particularly at the leading or distal stent edge (Fig. 8), suggesting that stent-based injury occurred at sharp transition points. In addition, as augmented protease signal was noted 1 to 2 mm away from the stent edge, another mechanism of vessel wall inflammation could be due to balloon extension (“overhang”) injury at the proximal and distal stent edges. Intriguingly, very high magnification *ex vivo* FRI of the resected coronary stents revealed increased cysteine protease activity at the greater curvature of stent struts (Figs. 9C to 9E).

The maximal SNR occurred at stent edges and was significantly greater than uninjured vessel segments for both *in vivo* NIRF pullbacks (median [quartiles]: 23.1 [11.7, 27.0] vs. 1.1 [1.0, 3.7], $p = 0.02$) and *ex vivo* FRI (median [quartiles]: 234.5 [160.6, 274.2] vs. 110.7 [100.7, 135.0], $p = 0.008$) (Figs. 9F and 9G). The maximum stent TBR was 18.3 [2.8, 25.7] in the VM110 group versus 1.2 [1.0, 1.4] in the saline group ($p = 0.056$) for the *in vivo* NIRF pullbacks. Immunoblot analyses also revealed augmented cathepsin B proteases in extracts of injured vessel wall encasing implanted coronary stents (Fig. 9H).

Discussion

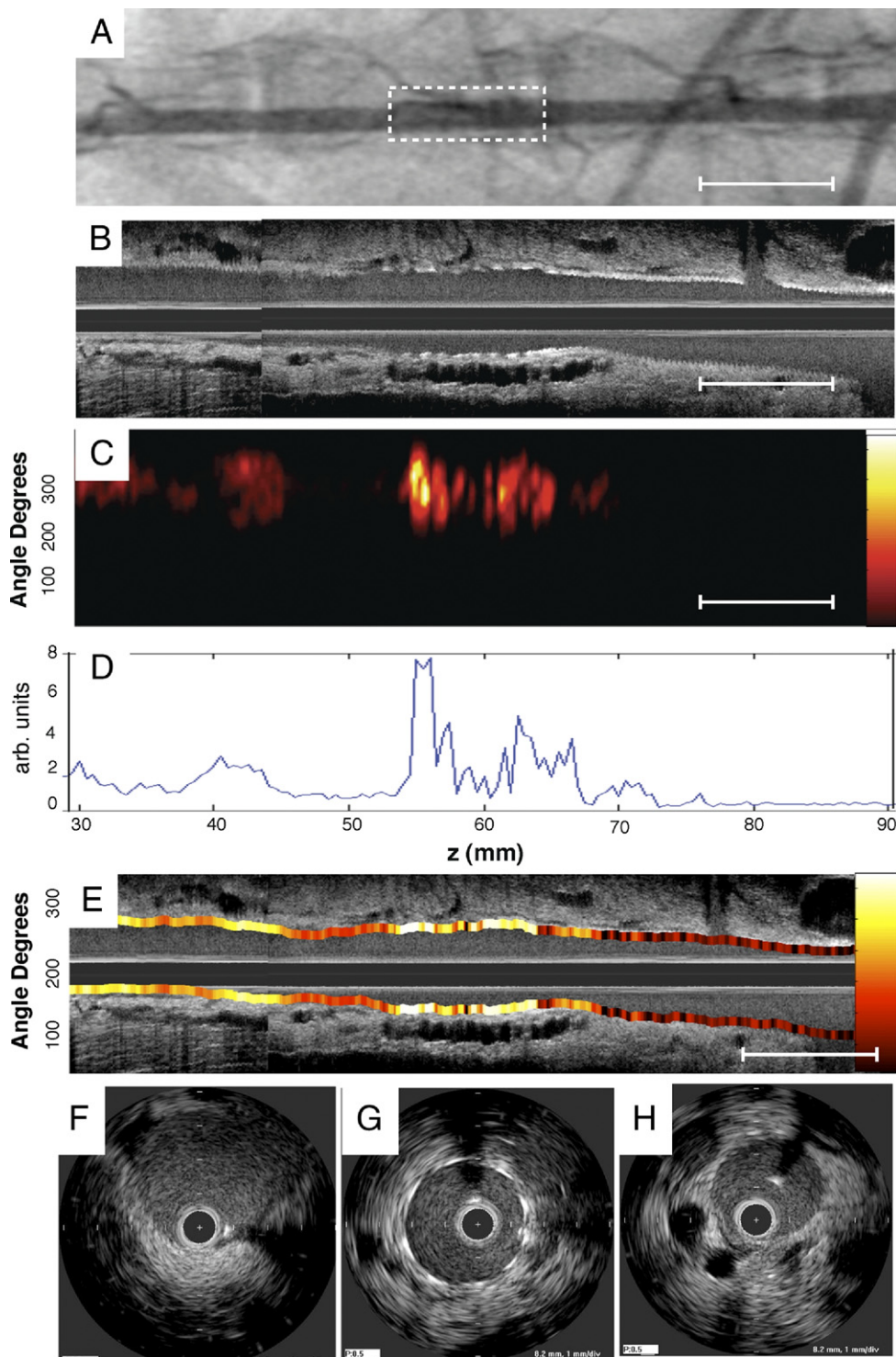
Complications of atherosclerosis and improperly healed coronary stents include acute myocardial infarction and sudden cardiac death. To address the unmet clinical need for high-resolution molecular imaging strategies targeted to coronary-sized arteries, we engineered and validated an intravascular catheter-based 2D NIRF imaging platform. The intravascular molecular imaging results demonstrate spatial mapping of arterial inflammation (as mediated by VM110 activation and fluorescence generation following cleavage by cysteine proteases) in atherosclerosis, as well as in coronary-stent induced vascular injury and arterial dissection. Anatomically accurate images were obtained in real-time, through blood, and without the need for flushing or occlusion.

The optimized 2D NIRF imaging system demonstrated several advantages *in vivo* compared with a prior guidewire device (8) and a recent less-sensitive 2D prototype (11) that did not support *in vivo* molecular imaging. These advantages include: 1) the ability to obtain 2D molecular images of multifocal vascular inflammation with 360° coverage and accurate geometry; 2) the ability to image vascular inflammation in blood-filled arteries of 3.5-mm diameter, which is significantly larger than demonstrated previously (1.5 to 2.0 mm) (8), thereby offering greater applicability to vessels of the caliber of

human coronary arteries; 3) coregistration of high-resolution IVUS that enabled fusion molecular-anatomical imaging; and 4) implementation of a clinical-type 2.9-F monorail catheter that avoids loss of distal vessel guidewire access.

Intravascular NIRF can image biological processes of importance in atherosclerosis and stent healing including inflammation, angiogenesis, fibrin deposition, and remodeling (16). In atherosclerosis, inflammation is a key biological process that promotes atherogenesis and plaque rupture, and it characterizes high-risk, vulnerable plaques (1). In particular, proteinases participate as key mediators of inflammation, facilitating matrix degradation, remodeling, leukocyte recruitment, and elastic lamina breakdown. In conjunction with the NIRF molecular imaging agent Prosense VM110, the intravascular NIRF catheter enabled high-resolution imaging of cysteine proteinase activity in atheromata, stent injury, and intimal dissection induced by arterial intervention. Subsequent histological and biochemical analyses linked the NIRF signal to cysteine proteases, a marker of inflamed plaques. In addition, fluorescence microscopy revealed differences between NIRF imaging of enzyme activity and immunohistochemical detection of enzyme presence (Fig. 7). In contradistinction to the more extensive immunoreactive cathepsin B protein in the intima and media of early and advanced atheroma, NIRF-detected cysteine protease activity was restricted to the diseased intima of more established atheromata. Unlike IVUS and other structural imaging methods, NIRF imaging of atheroma assesses the activity of cathepsin B and related enzymes and, hence, provides insight into the *in vivo* biology of inflamed plaques.

Stent thrombosis, a clinical syndrome that often causes acute myocardial infarction and cardiac death, may occur from incompletely healed coronary stents, typically characterized by impaired endothelialization, inflammation, and fibrin deposition (3,4). At present, few approaches can visualize biological aspects of coronary-stent induced injury *in vivo*. The employed 2D NIRF strategy provided new insights into *in vivo* arterial inflammation following implantation of bare-metal coronary stents in rabbit aortas (Fig. 8). The stent edges showed higher proteinase activity signal, and high-magnification *ex vivo* FRI demonstrated proteinase activity largely on the outer (greater) curvature of the employed bare-metal stent. This effect may result from differential flow-mediated inflammation related to the configuration of the stent strut (17). The observed edge-based inflammatory injury patterns *in vivo* further support that stent geometry, design, and materials influence the risk of stent thrombosis and restenosis (18). Further studies may shed light on the differences in the temporal-spatial patterns of arterial inflammation surrounding implanted drug-eluting stents compared with implanted bare-metal stents. **Study limitations.** A limitation to the current intravascular NIRF approach is surface-weighting of the NIRF signal as a function of fiber-to-wall distance, particularly in light-attenuating blood. This aspect limits the depth resolution of

**Figure 8****Representative Multimodality NIRF Molecular and IVUS Anatomical Imaging of Arterial Inflammation at Day 7 Following Coronary Stent Implantation**

(A) Angiogram of an implanted bare-metal stent in the abdominal aorta. **Dotted rectangle** denotes stent position. **(B, C)** Longitudinal IVUS and NIRF catheter pullbacks demonstrate NIRF signal within the stent. NIRF signal collection was performed through blood without flushing, in 3.5-mm diameter vessels. **(D)** Corresponding 1-dimensional plot of the angle-averaged 2D NIRF signal at each axial point. **(E)** Longitudinal IVUS and NIRF fusion image (**yellow/white** = strongest NIRF signal intensity, **red/black** = lowest NIRF signal intensity). **(F to H)** Axial IVUS images from percutaneous transluminal coronary angioplasty alone, stent, and normal vessel zones, respectively. Abbreviations as in Figures 1 and 5.

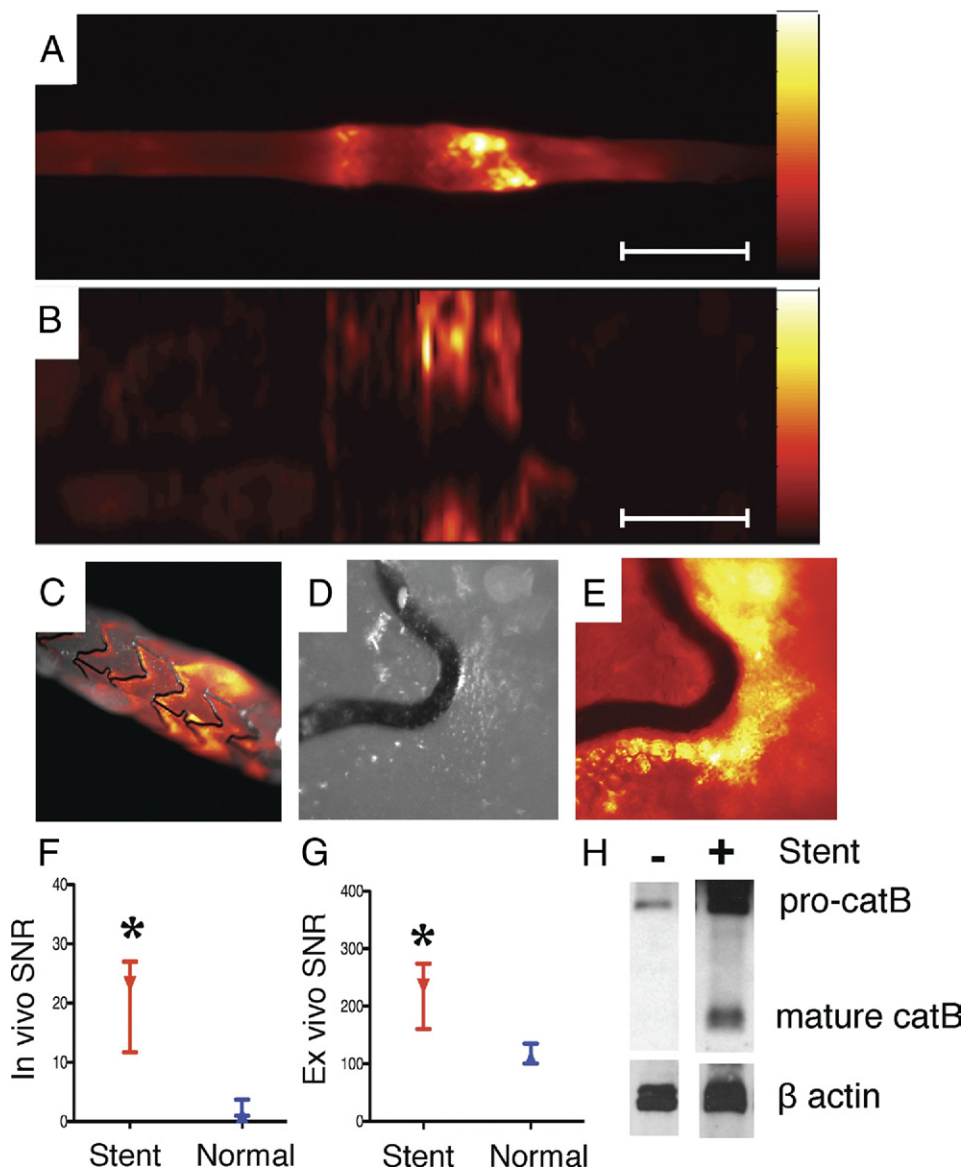


Figure 9 NIRF Imaging of Stent Injury

(A) Ex vivo FRI at 800 nm reveals augmented NIRF protease activity at stent edges. **(B)** Corresponding ex vivo intravascular NIRF pullback also detected stent-based NIRF signal increases. **(C)** Ex vivo NIRF-white light fusion image of the stent, **(D)** high-magnification white light, and **(E)** high-magnification NIRF image reveals signal along the greater curvature of stent struts. **(F)** In vivo and **(G)** ex vivo SNR in the normal and stented aorta (paired observations). **(H)** Immunoblot of cathepsin B (catB) staining in normal and stented rabbit aorta. Pro-catB denotes the 46 kDa pre-cathepsin B band, and mature catB denotes the 25 and 30 kDa cathepsin B bands. **Scale bar:** 10 mm. *p < 0.05. Abbreviations as in Figures 1, 2, and 3.

the NIRF signal, as well as optimal signal quantification for noncentered catheters. Possible compensation methods include the use of a focused fiber to image a more selective tissue volume, as well as mapping the luminal position of the NIRF catheter from coregistered IVUS information, as a first approximation, to correct the NIRF signal based on the fiber-to-wall distance. Of note is that plaque tissue is less likely to attenuate NIRF signals, based on prior tissue phantom studies (8). Additional sensitivity gains are anticipated with the use of focused and larger numerical aperture

fibers to deliver and collect light more efficiently. Finally, to enable accurate angular NIRF and IVUS coregistration, a limitation of the 2 separate NIRF and IVUS catheters, as well as additional strategies employing 3-dimensional radiopaque fiducials may be helpful.

Conclusions

From a translational standpoint, intracoronary NIRF molecular imaging via optical catheters appears clinically viable,

based on U.S. Food and Drug Administration approval of other light-based catheter approaches including optical coherence tomography/optical frequency domain imaging (19) and NIR spectroscopic chemical imaging (20) using similar laser powers and catheter sizes. In addition, clinical approval of NIRF imaging agents appears promising based on the favorable safety profile of indocyanine green (21), a clinical NIR fluorochrome widely used in retinal angiography and historically in cardiac output studies. Clinical use of such novel imaging technologies will naturally first require safety studies of new NIRF imaging agents and intravascular catheters.

Ultimately, high-resolution molecular imaging of coronary arteries could provide a new approach to: 1) investigate the natural history of inflammation in a variety of coronary arterial pathologies, including atherosclerosis, stent-induced vascular injury, dissection, arteritis and allograft vasculopathy; 2) investigate novel pharmacotherapies designed to attenuate inflammation in coronary atherosclerosis; and 3) to provide an *in vivo* biological framework to identify subjects with high-risk plaques and high-risk coronary stents predisposed to thrombosis.

Acknowledgments

The authors thank Claudio Vinegoni, PhD; Guillermo Tearney, MD, PhD; Dana Brooks, PhD; and Elazer Edelman, MD, PhD, for helpful discussions. They also thank Yoshi Iwamoto, BS, for histopathological assistance; J. Luis Guerrero, BS, for assistance in surgical studies; Peter Waterman, BS, for assistance with FRI studies; and Robert W. Yeh, MD, MSc, for statistical assistance.

Reprint requests and correspondence: Dr. Farouc A. Jaffer, Massachusetts General Hospital, Cardiovascular Research Center, Simches Research Building, Room 3206, 185 Cambridge Street, Boston, Massachusetts 02114. E-mail: fjaffer@mgh.harvard.edu. OR Dr. Vasilis Ntziachristos, Institute for Biological and Medical Imaging, Technische Universität München and Helmholtz Zentrum München, Ingolstaedter Landstrasse 1, 85764 Neuherberg, Germany. E-mail: v.ntziachristos@tum.de.

REFERENCES

1. Libby P. Inflammation in atherosclerosis. *Nature* 2002;420:868–74.
2. Rader DJ, Daugherty A. Translating molecular discoveries into new therapies for atherosclerosis. *Nature* 2008;451:904–13.
3. Luscher TF, Steffel J, Eberli FR, et al. Drug-eluting stent and coronary thrombosis: biological mechanisms and clinical implications. *Circulation* 2007;115:1051–8.
4. Nakazawa G, Finn AV, Joner M, et al. Delayed arterial healing and increased late stent thrombosis at culprit sites after drug-eluting stent placement for acute myocardial infarction patients: an autopsy study. *Circulation* 2008;118:1138–45.
5. Jaffer FA, Libby P, Weissleder R. Molecular imaging of cardiovascular disease. *Circulation* 2007;116:1052–61.
6. Sanz J, Fayad ZA. Imaging of atherosclerotic cardiovascular disease. *Nature* 2008;451:953–7.
7. Calfon MA, Vinegoni C, Ntziachristos V, Jaffer FA. Intravascular near-infrared fluorescence molecular imaging of atherosclerosis: toward coronary arterial visualization of biologically high-risk plaques. *J Biomed Opt* 2010;15:011107.
8. Jaffer FA, Vinegoni C, John MC, et al. Real-time catheter molecular sensing of inflammation in proteolytically active atherosclerosis. *Circulation* 2008;118:1802–9.
9. Weissleder R, Tung CH, Mahmood U, Bogdanov A Jr. *In vivo* imaging of tumors with protease-activated near-infrared fluorescent probes. *Nat Biotechnol* 1999;17:375–8.
10. Chen J, Tung CH, Mahmood U, et al. *In vivo* imaging of proteolytic activity in atherosclerosis. *Circulation* 2002;105:2766–71.
11. Razansky RN, Rosenthal A, Mallas G, Razansky D, Jaffer FA, Ntziachristos V. Near-infrared fluorescence catheter system for two-dimensional intravascular imaging *in vivo*. *Opt Express* 2010;18:11372–81.
12. Liu J, Sukhova GK, Sun J-S, Xu W-H, Libby P, Shi G-P. Lysosomal cysteine proteases in atherosclerosis. *Arterioscler Thromb Vasc Biol* 2004;24:1359–66.
13. Lutgens SP, Cleutjens KB, Daemen MJ, Heeneman S. Cathepsin cysteine proteases in cardiovascular disease. *FASEB J* 2007;21:3029–41.
14. Vinegoni C, Razansky D, Hilderbrand SA, Shao F, Ntziachristos V, Weissleder R. Transillumination fluorescence imaging in mice using biocompatible upconverting nanoparticles. *Opt Lett* 2009;34:2566–8.
15. Vinegoni C, Razansky D, Figueiredo JL, Nahrendorf M, Ntziachristos V, Weissleder R. Normalized Born ratio for fluorescence optical projection tomography. *Opt Lett* 2009;34:319–21.
16. Kim JW, Jaffer FA. Emerging molecular targets for intravascular imaging of high-risk plaques. *Curr Cardiovasc Imaging Rep* 2010;3:237–47.
17. Moore JE Jr. Biomechanical issues in endovascular device design. *J Endovasc Ther* 2009;16 Suppl 1:I1–11.
18. Rogers C, Edelman ER. Endovascular stent design dictates experimental restenosis and thrombosis. *Circulation* 1995;91:2995–3001.
19. Tearney GJ, Waxman S, Shishkov M, et al. Three-dimensional coronary artery microscopy by intracoronary optical frequency domain imaging. *J Am Coll Cardiol Img* 2008;1:752–61.
20. Waxman S, Dixon SR, L'Allier P, et al. *In vivo* validation of a catheter-based near-infrared spectroscopy system for detection of lipid core coronary plaques: initial results of the SPECTACL study. *J Am Coll Cardiol Img* 2009;2:858–68.
21. Hope-Ross M, Yannuzzi LA, Gragoudas ES, et al. Adverse reactions due to indocyanine green. *Ophthalmology* 1994;101:529–33.

Key Words: atherosclerosis ■ inflammation ■ intravascular imaging ■ molecular imaging ■ stent.

APPENDIX

For supplementary methods and figures,
please see the online version of this paper.